Analysis of Transient Electromagnetic Scattering Phenomena Using a Two-Level Plane Wave Time-Domain Algorithm

Balasubramaniam Shanker, *Member, IEEE*, A. Arif Ergin, *Student Member, IEEE*, Kemal Aygün, *Student Member, IEEE*, and Eric Michielssen, *Senior Member, IEEE*

***Abstract*—A fast algorithm is presented for solving electric, magnetic, and combined field time-domain integral equations pertinent to the analysis of surface scattering phenomena. The proposed two-level plane wave time-domain (PWTD) algorithm permits a numerically rigorous reconstruction of transient near fields from their far-field expansion and augments classical marching-on in-time (MOT) based solvers. The computational cost of analyzing surface scattering phenomena using PWTD-enhanced MOT schemes scales as $\mathcal{O}(N_t N_s^{3/2} \log N_s)$ as opposed to $\mathcal{O}(N_t N_s^2)$ for classical MOT methods, where N_t and N_s are the numbers of temporal and spatial basis functions discretizing the scatterer current. Numerical results that demonstrate the efficacy of the proposed solver in analyzing transient scattering from electrically large structures and that confirm the above complexity estimate are presented.**

***Index Terms*—Electromagnetic scattering, fast algorithms, integral equation methods, transient analysis.**

I. Introduction

NUMERICAL methods for analyzing electromagnetic transients find widespread engineering applications ranging from the analysis of broadband scattering to the design of modern antennas to the study of nonlinear phenomena and more. These simulators typically are based either on differential equations (DE's) [1], [2] or integral equations (IE's) [3]–[5]. Historically, DE methods have been favored over their integral equation (IE) counterparts (the vast majority of which are marching-on-in-time (MOT) methods [3]) as the latter often were found to be unstable [6] and highly expensive in application [7]. IE-based techniques, however, offer unmistakable advantages over DE-based methods when applied to the analysis of homogeneous/surface scatterers. First, IE solvers only require a discretization of the scatterer surface rather than a volume enclosing the latter, which results in a sharp decrease in the number of unknowns when compared to DE methods. Second, IE techniques automatically impose the radiation condition, hence, there is no need for (approximate local) absorbing boundary conditions that are required in the truncation of finite grids used by DE methods.

Manuscript received October 27, 1998; revised January 6, 2000. This work was supported in part by a grant from AFOSR via the MURI Program under Contract F49620-96-1-0025, NSF Grant ECS 95–02138, and the Gebze Institute of Technology.

The authors are with the Center for Computational Electromagnetics, Department of Electrical and Computer Engineering, University of Illinois at Urbana-Champaign, Urbana, IL 61801 USA.

Publisher Item Identifier S 0018-926X(00)03243-9.

Over the past several years, a considerable research effort has been expended on eliminating the aforementioned drawbacks of MOT solvers. Many a study has deepened our understanding of the origins of MOT instabilities and proposed new methods for confronting them (see [6], [8]–[12] and references therein). A series of recent papers by Walker's group demonstrates that MOT schemes for solving magnetic field integral equations "can be stabilized for all practical purposes" by relying on implicit time stepping methods [12], [13]. Impressive as progress on eliminating MOT instabilities is, the unfavorable scaling properties of MOT methods impedes their widespread use. Indeed, the cost of analyzing scattering using a classical MOT scheme for N_t time steps from an object whose surface current is discretized in terms of N_s spatial unknowns scales as $\mathcal{O}(N_t N_s^2)$. As a result, MOT solvers quickly swamp available computational resources when applied to large-scale scattering problems and reducing the computational complexity of time-domain IE schemes is imperative if these methods are to become truly competitive with DE schemes. Recently, Walker proposed a very interesting scheme for amortizing the costs of MOT schemes based on discounting noninteracting portions of a scatterer [14]. While this scheme has been successfully applied to the analysis of scattering from several interesting structures, it is heuristic in nature and a numerically rigorous technique for reducing the computational complexity of MOT solvers remains desirable.

The complexity problems associated with time domain IE methods are very similar to those that have for many years restricted the application of classical frequency-domain method of moments (MoM) solvers to large-scale scattering and radiation problems. However, these problems have been overcome by the fast multipole method (FMM), which achieves a very significant complexity reduction by expressing radiated fields in terms of a plane wave basis [15], [16]. Recently, we introduced scalar PWTD schemes—time-domain analogues of three-dimensional Helmholtz equation FMM methods—that enable the fast evaluation of transient scalar wave fields by decomposing radiated fields into transient plane waves. In these papers, it was theoretically shown that scalar PWTD methods used in conjunction with classical MOT schemes significantly reduce the computational complexity associated with the analysis of transient acoustic surface scattering phenomena [17], [18].

This article details a PWTD-enhanced MOT scheme with $\mathcal{O}(N_t N_s^{3/2} \log N_s)$ computational complexity for solving electric, magnetic, and combined field integral equations (EFIE,

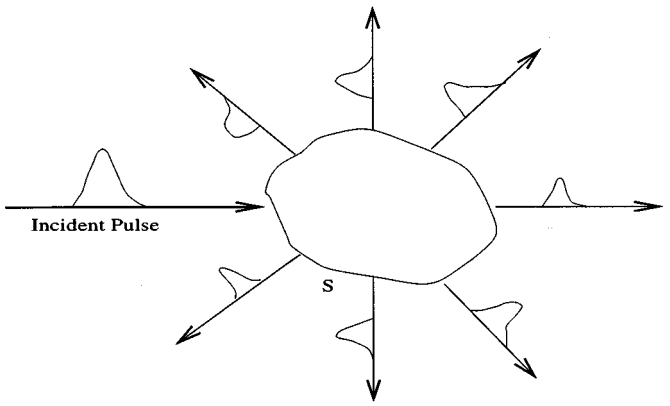

Fig. 1. Generic scattering problem description.

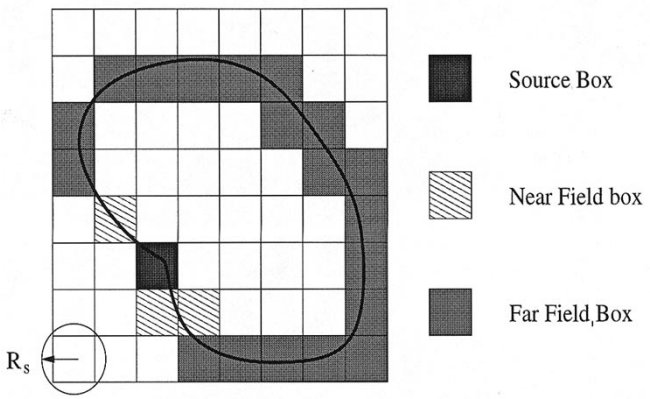

Fig. 2. Division of the geometry into near- and far-field blocks.

MFIE, CFIE) pertinent to the analysis of surface scattering phenomena. Within the context of this paper, the scheme is applied to the analysis of scattering from large perfect electrically conducting (PEC) objects that reside in free-space. And unless it is stated otherwise, all results are obtained using an implicit time-stepping scheme.

This paper will proceed as follows. Section II describes a time domain EFIE, MFIE, and CFIE, and classical MOT methods for solving these equations. Section III details the PWTD algorithm, its practical implementation within the context of an MOT solver, and the computational complexity of the resulting scheme. In Section IV the applicability of PWTD-enhanced MOT solvers to the analysis of scattering from electrically large structures is demonstrated, and the validity of the theoretical complexity estimates is experimentally verified. Section V presents our conclusions.

II. Formulation

In this section, three surface IE's for analyzing transient electromagnetic scattering phenomena—viz., an EFIE, an MFIE, and a CFIE—are introduced. In addition, an MOT scheme for solving these equations is presented along with a brief discussion of its stability properties.

A. Integral Equations

Consider a closed PEC body (Fig. 1) with surface S residing in free-space. In what follows, $\hat{\mathbf{n}}$ denotes an outward pointing position dependent normal to S, and S_- and S_+ are hypothetical surfaces that are conformal to but residing just inside and outside S, respectively. An impressed field with electric and magnetic components $\{\mathbf{E}^i(\mathbf{r},t),\mathbf{H}^i(\mathbf{r},t)\}$ that is temporally bandlimited to $f_{\max}$ impinges on S. The surface current $\mathbf{J}(\mathbf{r},t)$ that is induced on S by virtue of this interaction generates a scattered field $\{\mathbf{E}^s(\mathbf{r},t),\mathbf{H}^s(\mathbf{r},t)\}$ that is fully characterized by the vector potential $\mathbf{A}(\mathbf{r},t)$

$$\mathbf{A}(\mathbf{r},t)=\frac{\mu_0}{4\pi}\int_S dS'\,\frac{\mathbf{J}(\mathbf{r}',\tau)}{R} \tag{1}$$

where $R=|\mathbf{r}-\mathbf{r}'|$, $\tau=t-R/c$ denotes retarded time, c is the speed of light, and μ_0 is the permeability of free-space. In what follows, it is assumed that the incident field does not interact with S for $t\leq 0$, i.e., $\mathbf{J}(\mathbf{r},t)=0$ for $t\leq 0$.

A time-domain EFIE can be constructed by expressing the scattered electric field $\mathbf{E}^s(\mathbf{r},t)$ in terms of $\mathbf{A}(\mathbf{r},t)$ as

$$\mathbf{E}^s(\mathbf{r},t)=-\int_0^t dt'\,\left(\partial_{t'}^2\mathcal{I}-c^2\nabla\nabla\right)\cdot\mathbf{A}(\mathbf{r},t') \tag{2}$$

where $\mathcal{I}$ is the identity dyad. Enforcing the total electric field tangential to S to vanish (the same condition holds on both S_- and S_+) yields

$$\hat{\mathbf{n}}\times\hat{\mathbf{n}}\times\mathbf{E}^i(\mathbf{r},t)=-\hat{\mathbf{n}}\times\hat{\mathbf{n}}\times\mathbf{E}^s(\mathbf{r},t)\quad\forall\mathbf{r}\in S,S_-,S_+. \tag{3}$$

Combining (1)–(3) and denoting $\mathcal{V}_e\{\mathbf{E}^i(\mathbf{r},t),\mathbf{H}^i(\mathbf{r},t)\}=\hat{\mathbf{n}}\times\hat{\mathbf{n}}\times\mathbf{E}^i(\mathbf{r},t)$ results in the following EFIE:

$$\mathcal{V}_e\{\mathbf{E}^i(\mathbf{r},t),\mathbf{H}^i(\mathbf{r},t)\}=\mathcal{L}_e\{\mathbf{J}(\mathbf{r},t)\}\quad\forall\mathbf{r}\in S,S_-,S_+ \tag{4a}$$

where

$$\mathcal{L}_e\{\mathbf{J}(\mathbf{r},t)\}=\hat{\mathbf{n}}\times\hat{\mathbf{n}}\times\left\{\frac{\mu_0}{4\pi}\int_0^t dt'\int_S dS'\,\left(\partial_{t'}^2\mathcal{I}-c^2\nabla\nabla\right)\cdot\frac{\mathbf{J}(\mathbf{r}',t'-R/c)}{R}\right\}. \tag{4b}$$

Equation (4) not only holds true for closed S, but also for open structures.

A time-domain MFIE can be constructed by expressing the scattered magnetic field $\mathbf{H}^s(\mathbf{r},t)$ in terms of $\mathbf{A}(\mathbf{r},t)$ as

$$\mathbf{H}^s(\mathbf{r},t)=\frac{1}{\mu_0}\nabla\times\mathbf{A}(\mathbf{r},t) \tag{5}$$

and by enforcing the condition that the total magnetic field tangential to S_- vanishes, i.e.,

$$\hat{\mathbf{n}}\times\mathbf{H}^i(\mathbf{r},t)=-\hat{\mathbf{n}}\times\mathbf{H}^s(\mathbf{r},t)\quad\forall\mathbf{r}\in S_-. \tag{6}$$

Using (1), (5)–(6) and denoting $\mathcal{V}_h\{\mathbf{E}^i(\mathbf{r},t),\mathbf{H}^i(\mathbf{r},t)\}=\hat{\mathbf{n}}\times\mathbf{H}^i(\mathbf{r},t)$, the following MFIE can be derived [19]:

$$\mathcal{V}_h\{\mathbf{E}^i(\mathbf{r},t),\mathbf{H}^i(\mathbf{r},t)\}=\mathcal{L}_h\{\mathbf{J}(\mathbf{r},t)\}\quad\forall\mathbf{r}\in S_- \tag{7a}$$

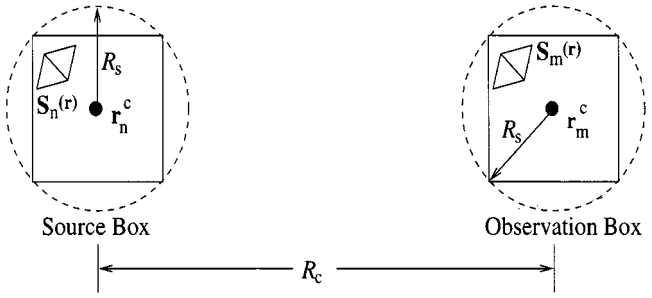

Fig. 3. Two far-field boxes (α, α') with basis functions $\mathbf{S}_n(\mathbf{r})$ and $\mathbf{S}_m(\mathbf{r})$.

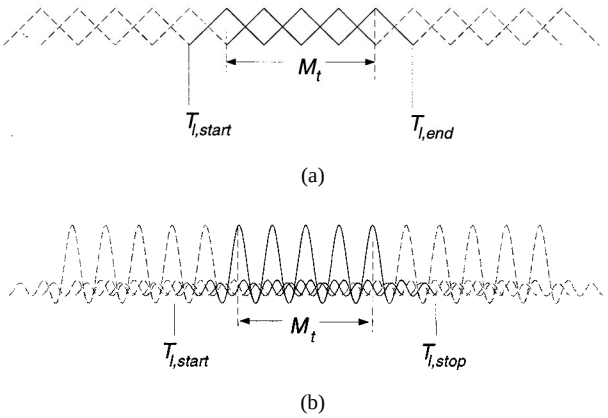

Fig. 4. Temporal basis functions (a) Triangular functions. (b) Approximate prolate spheroidal functions.

where

$$\mathcal{L}_h\{\mathbf{J}(\mathbf{r},\mathbf{t})\} = -\frac{1}{4\pi}\hat{\mathbf{n}} \times \int_S dS' \left[\frac{1}{cR^2}\partial_\tau \mathbf{J}(\mathbf{r}',\tau) + \frac{1}{R^3}\mathbf{J}(\mathbf{r}',\tau)\right] \times (\mathbf{r}-\mathbf{r}') \tag{7b}$$

where $\partial_\tau \mathbf{J}(\mathbf{r}',\tau) \Rightarrow \partial \mathbf{J}(\mathbf{r}',\mathbf{t})/\partial t|_{t=\tau}$.

It has recently been demonstrated that numerical solutions to the time-domain EFIE and MFIE, obtained using classical MOT solvers, are often corrupted by perturbed cavity modes when the spectrum of the incident field encompasses one or more of the scatterer's resonance frequencies [20]. While corruption by interior cavity modes are expected in the frequency-domain solutions to the EFIE and MFIE [19] (as the resonant currents satisfy the corresponding homogeneous differential equations), they are not expected in time domain as at $t = 0$ all fields are assumed to be zero. But, numerical time-marching schemes tend to "forget" [21] these initial conditions and the resonant modes are a component of the final solution. To combat this deficiency, a time-domain CFIE was introduced in [20] and its solutions shown to be free of resonant modes. Denoting, $\mathcal{V}_c\{\mathbf{E}^i(\mathbf{r},t),\mathbf{H}^i(\mathbf{r},t)\} = -\beta/\eta_0\mathcal{V}_e\{\mathbf{E}^i(\mathbf{r},t),\mathbf{H}^i(\mathbf{r},t)\} + \mathcal{V}_h\{\mathbf{E}^i(\mathbf{r},t),\mathbf{H}^i(\mathbf{r},t)\}$ where η_0 is the intrinsic impedance of free-space and β is a positive real constant, this CFIE reads

$$\mathcal{V}_c\{\mathbf{E}^i(\mathbf{r},t),\mathbf{H}^i(\mathbf{r},t)\} = \mathcal{L}_c\{\mathbf{J}(\mathbf{r},t)\} \quad \forall \mathbf{r} \in S_- \tag{8a}$$

where

$$\mathcal{L}_c\{\mathbf{J}(\mathbf{r},t)\} = -\beta/\eta_0\mathcal{L}_e\{\mathbf{J}(\mathbf{r},t)\} + \mathcal{L}_h\{\mathbf{J}(\mathbf{r},t)\}. \tag{8b}$$

B. Marching-On In-Time Formulation

This section develops a classical MOT-based scheme [6]–[22] for solving the integral equations ((4a), (7a), (8a)). Throughout this section, a subscript $q = e,h,c$ is used to represent quantities associated with the EFIE, MFIE, and CFIE, respectively. As a first step toward solving these equations using an MOT scheme, spatial, and temporal variations of the current $\mathbf{J}(\mathbf{r},t)$ are represented in terms of basis functions $\mathbf{S}_n(\mathbf{r})$, $n = 1,\cdots,N_s$, and $T_j(t)$, $j = 1,\cdots,N_t$ as

$$\mathbf{J}(\mathbf{r},t) = \sum_{j=1}^{N_t}\sum_{n=1}^{N_s} I_{n,j}\mathbf{S}_n(\mathbf{r})T_j(t). \tag{9}$$

Here, $I_{n,j}$ is the weight associated with the space-time basis function $\mathbf{S}_n(\mathbf{r})T_j(t)$. Denoting the surface area of the scatterer by S_a, the number of spatial basis functions is chosen as $N_s \propto S_a f_{\max}^2/c^2$ to ensure a discretization dense enough to represent the current at $f_{\max}$. Furthermore, assuming that $\mathbf{J}(\mathbf{r},t)$ resides on S for $0 < t < T$ and becomes vanishingly small thereafter, the number of temporal samples is chosen as $N_t \propto T f_{\max}$.

Rao–Wilton–Glisson (RWG) functions, which in the past have been used extensively in both frequency- and time-domain analysis [22], [23], are chosen to model the spatial variation of the current. To this end, S is approximated in terms of flat triangular panels and one basis function $\mathbf{S}_n(\mathbf{r})$ associated with each edge joining two triangles

$$\mathbf{S}_n(\mathbf{r}) = \begin{cases} \dfrac{l_n}{2A_n^+}\rho_n^+(\mathbf{r}), & \text{for } \mathbf{r} \in \Gamma_n^+ \\ \dfrac{l_n}{2A_n^-}\rho_n^-(\mathbf{r}), & \text{for } \mathbf{r} \in \Gamma_n^- \\ 0, & \text{elsewhere} \end{cases} \tag{10}$$

where l_n is the length of the common edge between the triangles Γ_n^+ and Γ_n^-, $A_n^\pm$ is the area of the triangle $\Gamma_n^\pm$, and $\rho_n^\pm(\mathbf{r})$ is the position vector with respect to the free vertex of the corresponding triangle [22]. Linearly interpolating (triangular) functions are used to represent the temporal variation of the current, i.e., $T_j(t) = T(t - j\Delta_t)$, where $\Delta_t = T/N_t$ is the time-step size and $T(t) = 1$ for $t = 0$ and linearly interpolates to zero at $t = \pm\Delta_t$.

Substituting (9) in (4), (7), (8) and using a spatial Galerkin testing procedure at $t_j = j\Delta_t$ leads to a set of equations that can be represented in matrix form as

$$\mathcal{Z}_q^0\mathcal{I}_j = \mathcal{F}_q^j - \sum_{i=1}^{j-1}\mathcal{Z}_q^i\mathcal{I}_{j-i} \tag{11a}$$

where $\mathcal{I}_j$ is an array of the weights $I_{n,j}, n = 1,\cdots,N_s$

$$\mathcal{F}_{q,m}^j = \langle \mathbf{S}_m(\mathbf{r}), \mathcal{V}_q\{\mathbf{E}^i(\mathbf{r},t),\mathbf{H}^i(\mathbf{r},t)\}\rangle|_{t=t_j} \tag{11b}$$

and

$$\mathcal{Z}_{q,mn}^i = \langle \mathbf{S}_m(\mathbf{r}), \mathcal{L}_q\{\mathbf{S}_n(\mathbf{r})T_{j-i}(t)\}\rangle|_{t=t_j}. \tag{11c}$$

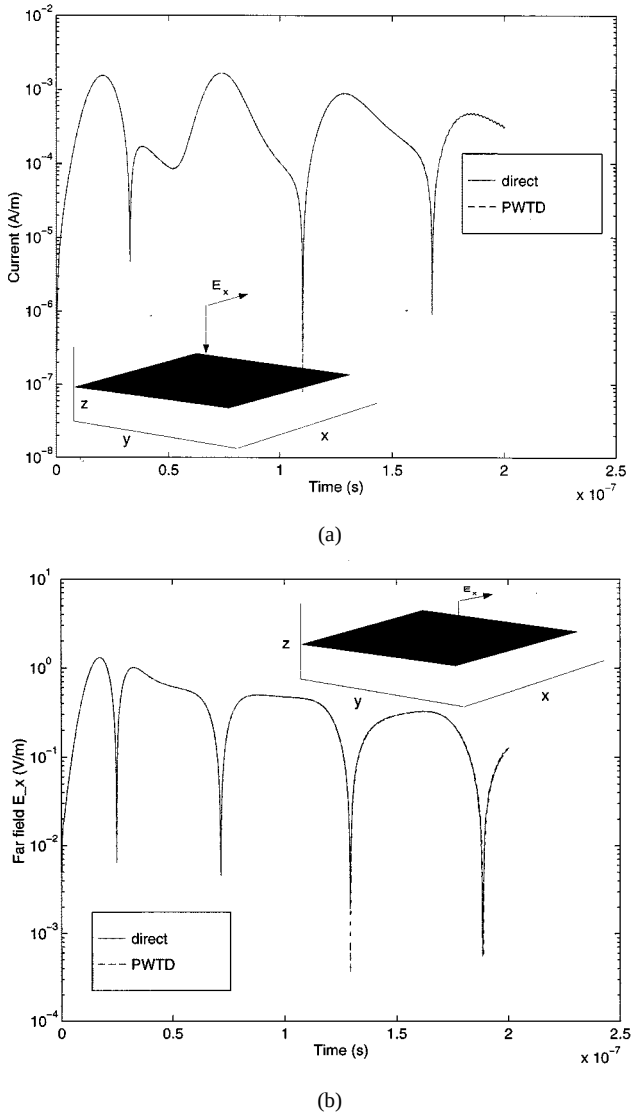

Fig. 5. Transient scattering from a plate analyzed using the EFIE. The plate is discretized with 2170 unknowns. The plate measures 2 m × 15 m. The incident field is $\hat{\mathbf{k}} = -\hat{\mathbf{z}}$ directed and $\hat{\mathbf{p}} = \hat{\mathbf{x}}$ polarized. (a) Current at a location on the plate. (b) The backscattered far-field E_x.

In the above equations $\langle \cdot, \cdot \rangle$ denotes the standard inner product [22]. Equation (11a) constitutes the basis of the classical MOT scheme; it relates the currents on the surface at t_j to those at $t \leq t_{j-1}$ and, hence, permits the recursive computation of currents for all times.

Until recently, all MOT schemes were prone to late time instabilities. A vast body of literature on the analysis of, and remedies for addressing, these instabilities exists (see [6], [22], [24], [25] and references therein). Rynne and Smith [6] provide an insightful explanation of the origin of these instabilities and suggest averaging schemes to stabilize the MOT procedure. Their analysis hinges on the location and movement of the poles of the resolvent of the integral operator $\mathcal{L}_q$ [21]. More recently, Dodson *et al.* observed that use of an implicit time stepping procedure stabilizes the MOT procedure "for all practical purposes" [13]. It has also been suggested that the stability of MOT schemes can be further improved by relying on backward temporal differencing and higher order temporal basis functions [25].

In our implementation, all inner products are evaluated by using seven-point Gaussian quadrature rules over triangular domains [23]. This testing procedure leads to an implicit scheme, even for the time-step size suggested in [22]. In our implementation, the time-step size chosen is independent of the spatial discretization and is $\Delta_t = \alpha/(10 f_{\max})$, where $\alpha \geq 1$. The resulting scheme is termed implicit because $\mathcal{Z}_q^0$ is not diagonal. However, as this matrix is highly sparse, a nonstationary iterative solver such as quasi-minimal residual (QMR) [26] can be used to efficiently solve for $\mathcal{I}_j$ each and every time step. The additional cost incurred from the use of such a solver is insignificant when compared to the overall cost. In addition to implicit time stepping, accurate spatial and temporal integration rules are used for computing $\mathcal{L}_q\{\mathbf{J}(\mathbf{r}, t)\}$ [12], [27].

The dominant cost in the construction of (11a) involves the vector sum that appears on its right-hand side. The cost of evaluating this sum scales as $\mathcal{O}(N_s^2)$; indeed the reaction at any testing point comprises of contributions from all N_s source basis functions. Since this sum is evaluated for all N_t time steps, the total cost of this analysis scales as $\mathcal{O}(N_t N_s^2)$. In the next section, a succinct derivation of the two-level PWTD algorithm that results in a reduction of this cost will be presented and details regarding its implementation into existing MOT codes will be outlined.

III. Plane Wave Time-Domain Algorithm

From the proceeding discussion, it is apparent that computing interactions between individual basis functions, as in traditional MOT schemes, leads to a computationally inefficient algorithm. This suggests that one of the keys to developing a reduced-complexity algorithm is constructing schemes that permit the computation of interactions in a group-wise manner. To this end, assume that the scatterer can be enclosed in a fictitious cubical box which is further subdivided in many smaller equal-sized cubes or boxes (Fig. 2). The radius of a sphere circumscribing each cube is denoted by R_s and the set of basis functions, which are contained in a box is called a group. Then, all nonempty boxes are identified and numbered from $\alpha = 1, \cdots, N_g$. Next, a pair of boxes (α, α') is classified as either a "near-field" or "far-field" pair, depending on a separation criterion based on the distance between the box centers. In our analysis, this distance was chosen to be $R_{c,\min} < \gamma R_s$, where $4 \leq \gamma \leq 6$. Since $R_{c,\min} = \mathcal{O}(R_s)$, the number of near-field pairs is proportional to the total number of nonempty boxes N_g. The interactions between the basis functions that reside in a near-field box pair are computed using the classical MOT scheme. However, the interactions between those that reside in a far-field box pair are computed in a group-wise manner using the PWTD algorithm. The foundations of the PWTD algorithm lie in expressing the field at a point due to a sufficiently separated source distribution as a superposition of plane waves. Such a representation, as in the FMM, has been extremely effective in reducing the computational complexity of the frequency domain IE solvers. Consequently, the analysis in the first part of this section will

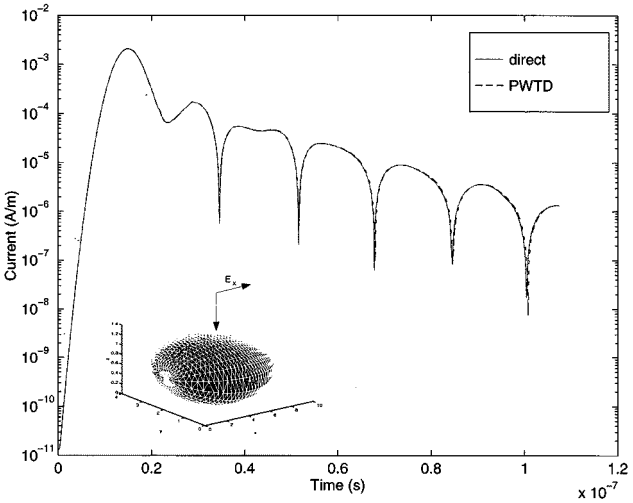

(a)

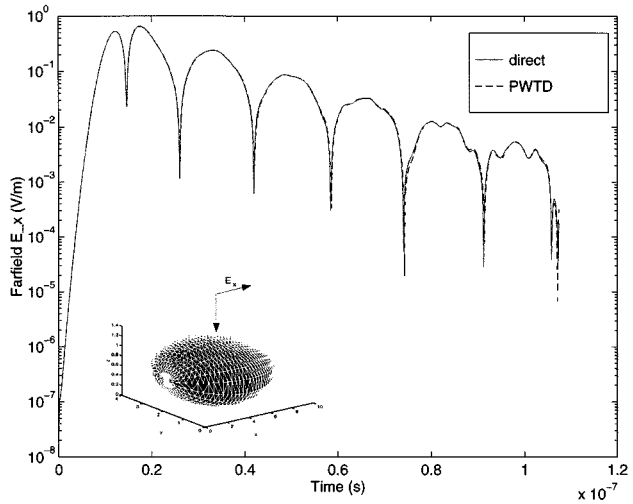

(b)

Fig. 6. Transient scattering from an almond, which is discretized using 4680 spatial basis functions, analyzed using the MFIE. The incident field propagates along $\hat{\mathbf{k}} = -\hat{\mathbf{z}}$ and is $\hat{\mathbf{p}} = \hat{\mathbf{x}}$ polarized. (a) Current at a location on the almond. (b) The backscattered far-field E_x.

focus on the development of such a scheme in the time domain. Next, the incorporation of this algorithm into an MOT scheme in a two-level setting is elucidated. Finally, it is shown that the resulting PWTD-enhanced MOT algorithm has a computational complexity of $\mathcal{O}(N_t N_s^{3/2} \log N_s)$.

A. Plane Wave Representations

Consider a far-field box pair as shown in Fig. 3, one of which contains the basis function $\mathbf{S}_n(\mathbf{r})$ and is dubbed the source box, the other contains the basis function $\mathbf{S}_m(\mathbf{r})$ and is called the observation box. The centers of these boxes are located at $\mathbf{r}_n^c$ and $\mathbf{r}_m^c$, respectively. The vector connecting the centers of these boxes is denoted by $\mathbf{R}_c = \mathbf{r}_m^c - \mathbf{r}_n^c$ and $R_c = |\mathbf{R}_c|$. For the purpose of this exposition, let the current associated with the source basis function be characterized as

$$\mathbf{J}_n(\mathbf{r},t) = \sum_{j=1}^{N_t} I_{n,j}\mathbf{S}_n(\mathbf{r})T_j(t) = \mathbf{S}_n(\mathbf{r})f_n(t). \tag{12}$$

The time signature $f_n(t)$ is divided into L consecutive subsignals $f_{n,l}(t)$, each of duration $T_s = (M_t+1)\Delta_t$ (with $LM_t = N_t$) occupying a time slice $T_{l,\text{start}} \le t \le T_{l,\text{stop}}$ for $l = 1,\cdots,L$, where $T_{l,\text{start}} = (l-1)M_t\Delta_t$, and $T_{l,\text{stop}} = lM_t\Delta_t + \Delta_t$ (see Fig. 4(a)). In keeping with this division, the current source $\mathbf{J}_n(\mathbf{r},t)$ can be rewritten as

$$\mathbf{J}_n(\mathbf{r},t) = \sum_{l=1}^{L}\mathbf{J}_{n,l}(\mathbf{r},t) \tag{13a}$$

where

$$\mathbf{J}_{n,l}(\mathbf{r},t) = \mathbf{S}_n(\mathbf{r})f_{n,l}(t);$$
$$f_{n,l}(t) = \sum_{j=(l-1)M_t+1}^{lM_t} I_{n,j}T_j(t). \tag{13b}$$

Then, the vector potential associated with one subsignal is

$$\mathbf{A}_{n,l}(\mathbf{r},t) = \frac{\mu_0}{4\pi}\int_{S_n} dS'\,\frac{\mathbf{S}_n(\mathbf{r}')f_{n,l}(t-R/c)}{R}. \tag{14}$$

Alternatively, motivated by frequency-domain fast multipole methods that rely heavily on plane wave expansions, consider the field

$$\tilde{\mathbf{A}}_{n,l}(\mathbf{r},t) = -\frac{\mu_0\partial_t}{8\pi^2 c}\int d^2\Omega \int_{S_n} dS'\,\mathbf{S}_n(\mathbf{r}') \times \delta(t-\hat{\mathbf{k}}\cdot(\mathbf{r}-\mathbf{r}')/c) * f_{n,l}(t) \tag{15a}$$

where $\hat{\mathbf{k}} = \hat{\mathbf{x}}\sin\theta\cos\phi + \hat{\mathbf{y}}\sin\theta\sin\phi + \hat{\mathbf{z}}\cos\theta$, $*$ denotes a temporal convolution and

$$\int d^2\Omega \doteq \int_0^{2\pi} d\phi \int_0^{\pi} d\theta \sin\theta. \tag{15b}$$

To relate $\tilde{\mathbf{A}}_{n,l}(\mathbf{r},t)$ to the vector potential $\mathbf{A}_{n,l}(\mathbf{r},t)$, the spectral integral in (15a) is evaluated by interchanging the order of integrations and transforming the spatial variables to a new coordinate system in which $\hat{\mathbf{z}}'$ is parallel to $\mathbf{R}$. Defining θ' and ϕ' as the angular coordinates in this new system, (15a) reduces to [28], [29]

$$\begin{aligned}\tilde{\mathbf{A}}_{n,l}(\mathbf{r},t) &= -\frac{\mu_0\partial_t}{8\pi^2 c}\int_{S_n} dS' \int_0^{2\pi} d\phi' \int_0^{\pi} d\theta' \sin\theta' \mathbf{S}_n(\mathbf{r}') \\ &\quad\times f_{n,l}\left(t - \frac{R}{c}\cos\theta'\right) \\ &= -\frac{\mu_0\partial_t}{8\pi^2}\int_{S_n} dS' \int_0^{2\pi} d\phi \int_{-R/c}^{R/c} d\tau \\ &\quad\times \frac{\mathbf{S}_n(\mathbf{r}')f_{n,l}(t-\tau)}{R} \\ &= \frac{\mu_0}{4\pi}\int_{S_n} dS'\,\frac{\mathbf{S}_n(\mathbf{r}')f_{n,l}(t-R/c)}{R} \\ &\quad - \frac{\mu_0}{4\pi}\int_{S_n} dS'\,\frac{\mathbf{S}_n(\mathbf{r}')f_{n,l}(t+R/c)}{R}.\end{aligned} \tag{16}$$

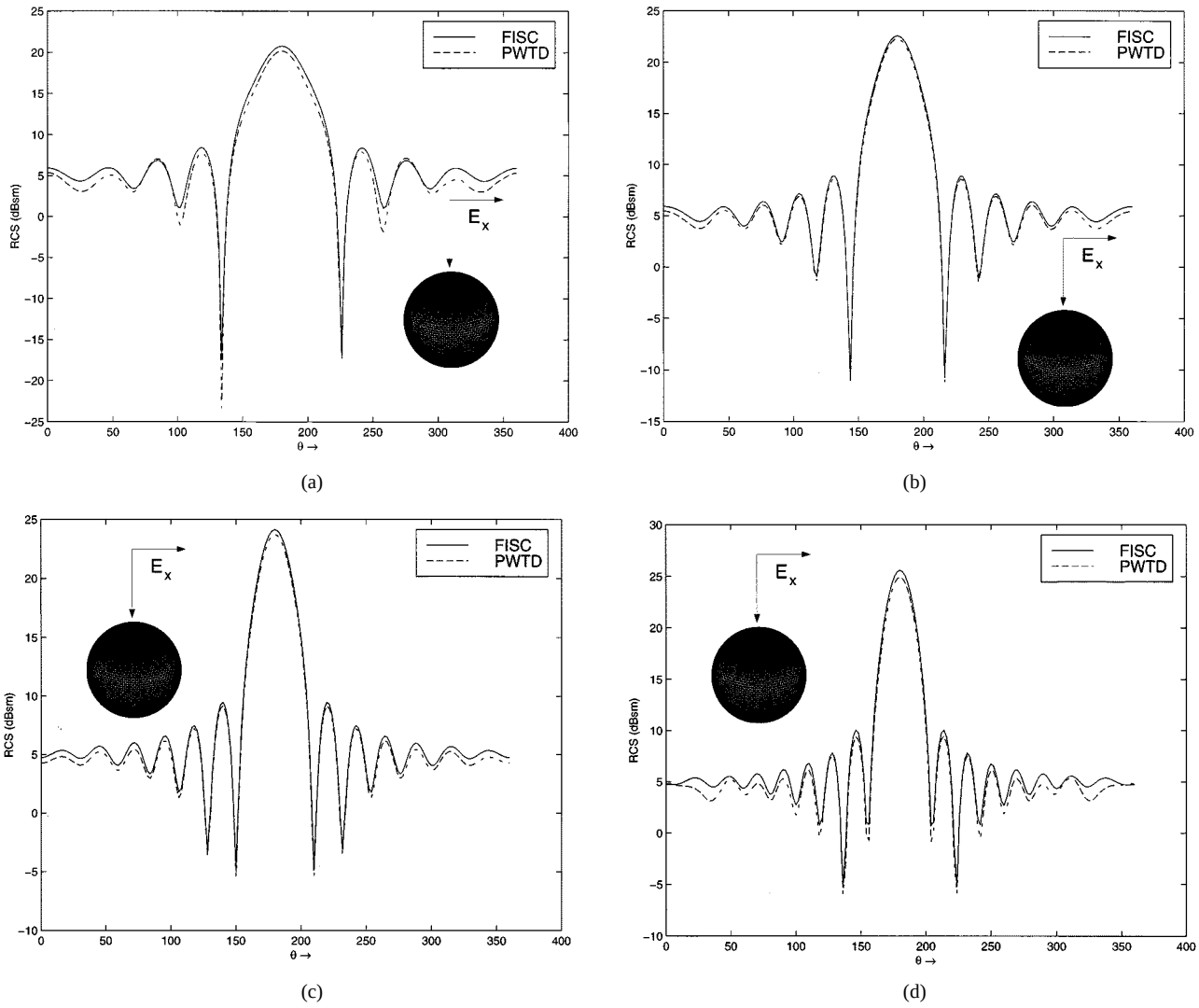

Fig. 7. Radar cross section of a sphere in the z-x plane extracted from the time-domain CFIE result is compared to that obtained from FISC for four different frequencies. The incident wave propagates along $\hat{\mathbf{k}} = -\hat{\mathbf{z}}$ and is $\hat{\mathbf{p}} = \hat{\mathbf{x}}$ polarized and the sphere is discretized using 9414 spatial basis functions. (a) 280 MHz. (b) 350 MHz. (c) 420 MHz. (d) 500 MHz.

Comparing (14) and (16), it is apparent that the evaluation of (15a) yields the true vector potential (first term) and an anti-causal signal (second term), which will henceforth be referred to as the ghost signal. As the ghost signal appears at the observer before the true signal arrives, it is possible to time-gate $\tilde{\mathbf{A}}_{n,l}(\mathbf{r},t)$ and recover the true vector potential provided that certain conditions are met.

To develop a scheme for time-gating $\tilde{\mathbf{A}}_{n,l}(\mathbf{r},t)$, the following observations are in order. With reference to (16), the true vector potential radiated by the subsignal $f_{n,l}(t)$ reaches the observer no sooner than $t = T_{l,\text{start}} + \min\{R\}/c$, and the ghost signal vanishes after $t = T_{l,\text{stop}} - \min\{R\}/c$. Hence, choosing the duration of the signal $T_s < \min\{R\}/c$ implies that $f_{n,l}(t)$ vanishes before the true signal reaches the observer and that the ghost and true fields never overlap in time. These observations can now be generalized for an arbitrary distribution of sources and observers residing in their respective spheres. For this configuration, the arrival of the true signal can be no sooner than $(R_c - 2R_s)/c$ following the onset of a source signal at $t = T_{l,\text{start}}$. Hence, the choice $T_s < (R_c - 2R_s)/c$ dictates that $\mathbf{A}_{n,l}(\mathbf{r},t) = 0$ for $t < T_{l,\text{stop}}$ and $\mathbf{A}_{n,l}(\mathbf{r},t) = \tilde{\mathbf{A}}_{n,l}(\mathbf{r},t)$ for $t \geq T_{l,\text{stop}}$ as the ghost signal vanishes for $t > -(R_c - 2R_s)/c + T_{l,\text{stop}}$. Summarizing these observations, the choice of $T_s < (R_c - 2R_s)/c$ ensures that

$$\mathbf{A}_{n,l}(\mathbf{r},t) = \begin{cases} 0, & \text{for } t < T_{l,\text{stop}} \\ \tilde{\mathbf{A}}_{n,l}(\mathbf{r},t), & \text{for } t \geq T_{l,\text{stop}}. \end{cases} \tag{17}$$

It follows that both the electric and magnetic fields can be evaluated from (15a). Indeed, using (2) and (5) and the fact that $\nabla \Leftrightarrow -\partial_t \hat{\mathbf{k}}/c$ holds for plane wave basis, the fields in the observation sphere due to the lth source time slice for $t > T_{l,\text{stop}}$ can be written as

$$\mathbf{E}^s_{n,l}(\mathbf{r},t) = \frac{\eta_0}{8\pi^2 c^2} \int_{T_{l,\text{stop}}}^{t} dt' \, \partial_{t'}^3 \int d^2\Omega \, (\mathcal{I} - \hat{\mathbf{k}}\hat{\mathbf{k}}) \cdot \int_{S_n} dS' \, \mathbf{S}_n(\mathbf{r}') \delta(t' - \hat{\mathbf{k}} \cdot (\mathbf{r} - \mathbf{r}')/c) * f_{n,l}(t') \tag{18a}$$

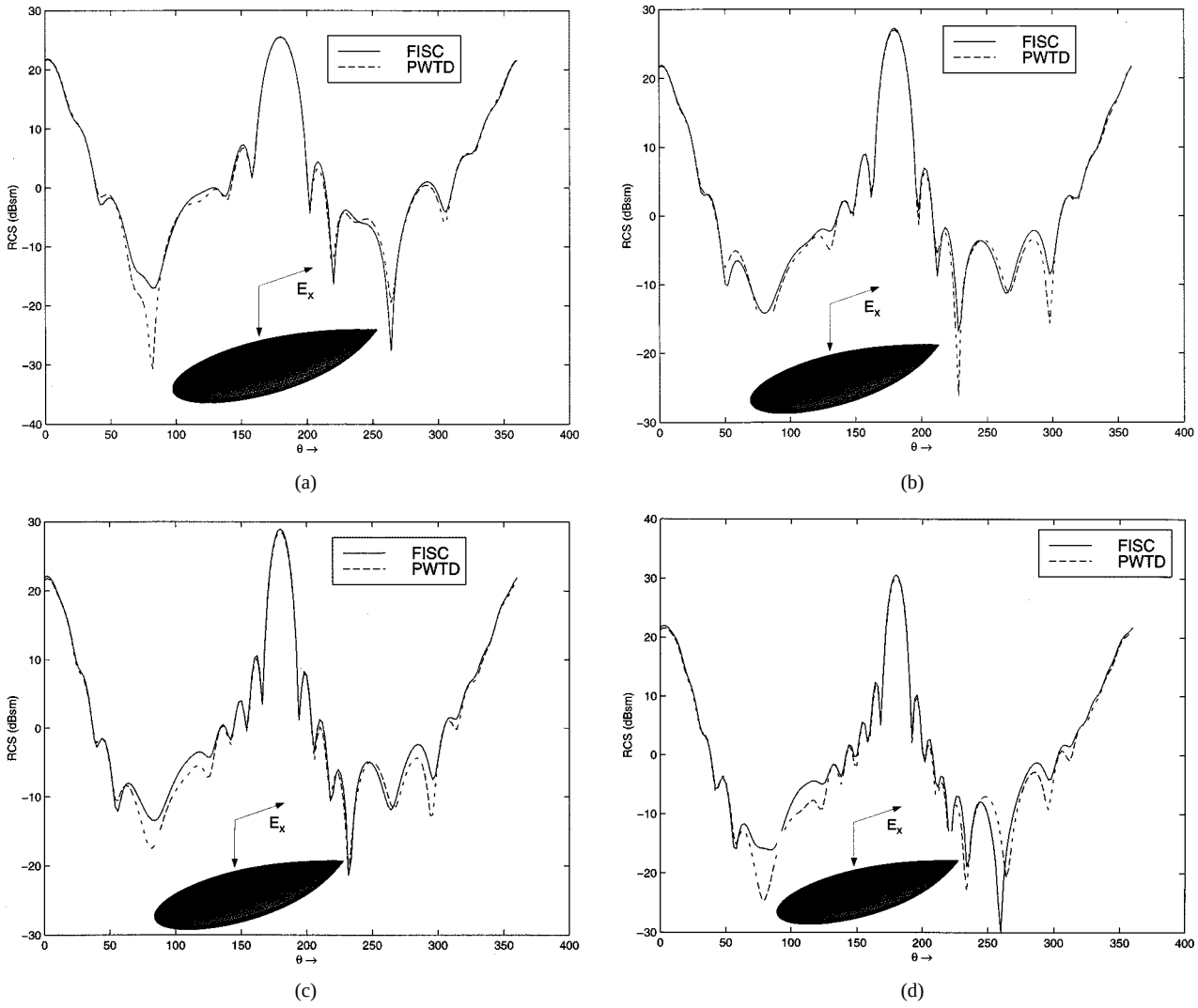

Fig. 8. Radar cross section of an almond in the z-x plane extracted from the time-domain CFIE result is compared to that obtained from FISC for four different frequencies. The incident wave propagates along $\hat{\mathbf{k}} = -\hat{\mathbf{z}}$ and is $\hat{\mathbf{p}} = \hat{\mathbf{x}}$ polarized and the almond is discretized using 10 620 spatial basis functions. (a) 210.2 MHz. (b) 261.8 MHz. (c) 322 MHz. (d) 390.8 MHz.

$$\mathbf{H}^s_{n,l}(\mathbf{r},t) = \frac{1}{8\pi^2 c^2}\int_{Tl,\text{stop}}^{t} dt'\,\partial_{t'}^3 \int d^2\Omega\,\hat{\mathbf{k}} \times \int_{S_n} dS'\,\mathbf{S}_n(\mathbf{r}')\delta(t'-\hat{\mathbf{k}}\cdot(\mathbf{r}-\mathbf{r}')/c) * f_{n,l}(t'). \tag{18b}$$

Equations (18) indicate that the scattered electric and magnetic fields can be constructed using the transverse components of the vector potential. It should also be noted that the time integrals in (18) should not be cancelled by one of the time derivatives that follow as this will introduce an undesirable static ghost signal.

To explore the merits of a plane wave representation in constructing a fast algorithm, note that $\tilde{\mathbf{A}}(\mathbf{r},t)$ tested with a basis function $\mathbf{S}_m(\mathbf{r})$ can be written as

$$\langle \mathbf{S}_m(\mathbf{r}), \tilde{\mathbf{A}}(\mathbf{r},t)\rangle = -\frac{\mu_0\partial_t}{8\pi^2 c}\int d^2\Omega \times \left[\int_{S_m} dS\,\mathbf{S}_m(\mathbf{r})\delta\left(t-\hat{\mathbf{k}}\cdot(\mathbf{r}-\mathbf{r}_m^c)/c\right)\right]^T * \delta(t-\hat{\mathbf{k}}\cdot\mathbf{R}_c/c) * \left[\int_{S_n} dS'\,\mathbf{S}_n(\mathbf{r}')\delta\left(t+\hat{\mathbf{k}}\cdot(\mathbf{r}'-\mathbf{r}_n^c)/c\right)\right] * f_{n,l}(t) \tag{19}$$

for $t > T_{l,\text{stop}}$, where the superscript T is used to denote a transpose. Similarly, using (4), (7), (8), (18), it can be shown that the inner products of the fields $\mathbf{E}^s_{n,l}(\mathbf{r},t)$ and $\mathbf{H}^s_{n,l}(\mathbf{r},t)$ with $\mathbf{S}_m(\mathbf{r})$ are zero for $t < T_{l,\text{stop}}$ and for $t \geq T_{l,\text{stop}}$

$$\langle \mathbf{S}_m(\mathbf{r}), \mathcal{L}_e\{\mathbf{J}_{n,l}(\mathbf{r},t)\}\rangle = \frac{\eta_0}{8\pi^2 c^2}\int_{T_{l,\text{stop}}}^{t} dt' \int d^2\Omega\,[\mathcal{S}_m^-(\hat{\mathbf{k}},t',\hat{\mathbf{k}})]^T * \mathcal{T}(\hat{\mathbf{k}},t') * [\mathcal{S}_n^+(\hat{\mathbf{k}},t',\hat{\mathbf{k}})] * f_{n,l}(t') \tag{20a}$$

$$\langle \mathbf{S}_m(\mathbf{r}), \mathcal{L}_h\{\mathbf{J}_{n,l}(\mathbf{r},t)\}\rangle = \frac{1}{8\pi^2 c^2}\int_{T_{l,\text{stop}}}^{t} dt' \int d^2\Omega\,[\mathcal{S}_m^-(\hat{\mathbf{k}},t',\hat{\mathbf{n}})]^T * \mathcal{T}(\hat{\mathbf{k}},t') * [\mathcal{S}_n^+(\hat{\mathbf{k}},t',\hat{\mathbf{k}})] * f_{n,l}(t') \tag{20b}$$

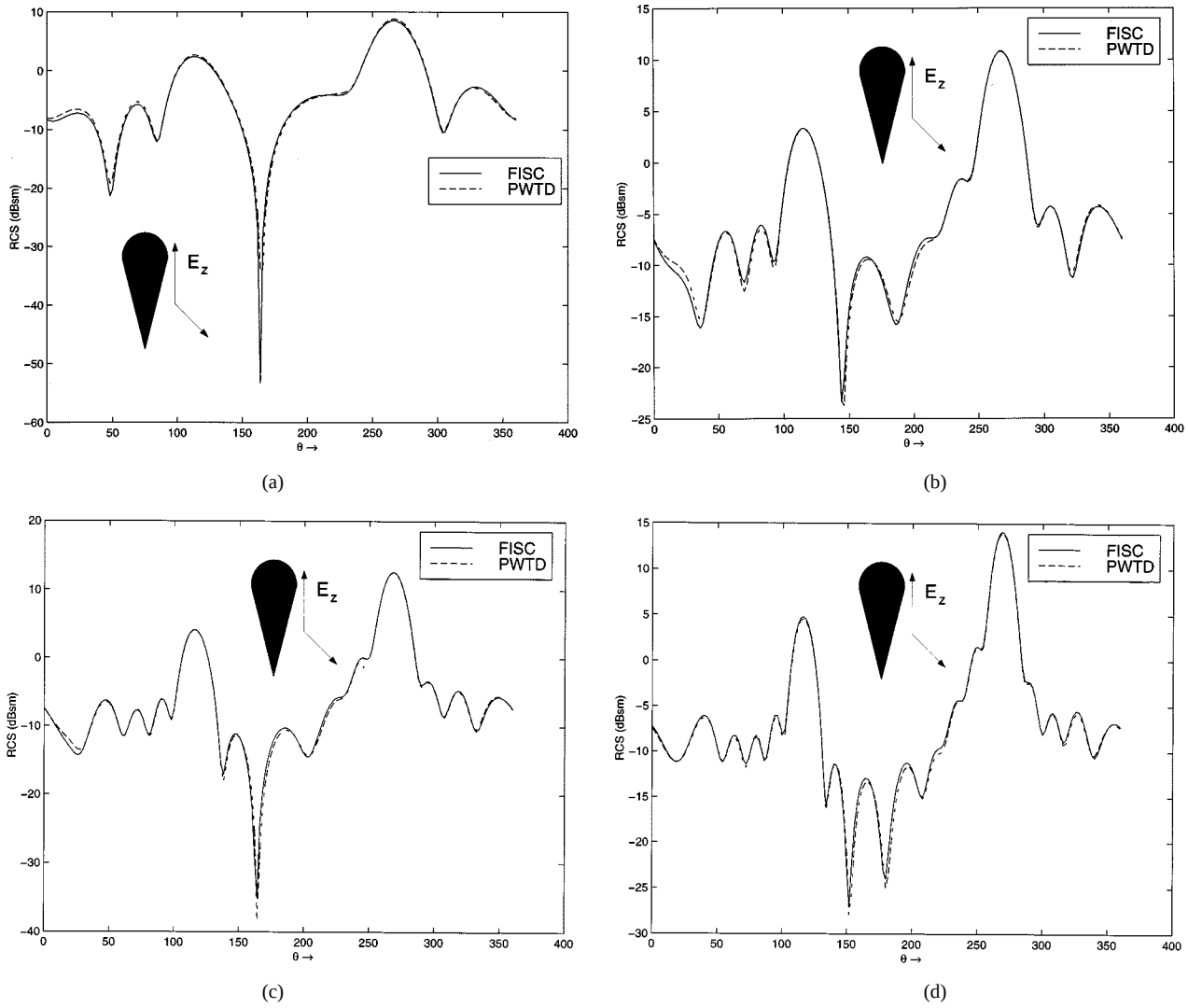

Fig. 9. Radar cross section of a cone sphere in the z-y plane extracted from the time-domain CFIE result is compared to that obtained from FISC for four different frequencies. The incident wave propagates along $\hat{\mathbf{k}} = -\hat{\mathbf{y}}$ and is $\hat{\mathbf{p}} = \hat{\mathbf{z}}$ polarized and the cone sphere is discretized using 11 412 spatial basis functions. (a) 500 MHz. (b) 700 MHz. (c) 900 MHz. (d) 1100 MHz.

and

$$\langle \mathbf{S}_m(\mathbf{r}), \mathcal{L}_c\{\mathbf{J}_{n,l}(\mathbf{r},t)\}\rangle = -\frac{\beta}{\eta_0}\langle \mathbf{S}_m(\mathbf{r}), \mathcal{L}_e\{\mathbf{J}_{n,l}(\mathbf{r},t)\}\rangle + \langle \mathbf{S}_m(\mathbf{r}), \mathcal{L}_h\{\mathbf{J}_{n,l}(\mathbf{r},t)\}\rangle. \quad (20c)$$

In the above equations, $\mathcal{T}(\hat{\mathbf{k}},t)$ denotes the translation function

$$\mathcal{T}(\hat{\mathbf{k}},t) = \partial_t^3 \delta(t - \hat{\mathbf{k}}\cdot\mathbf{R}_c/c) \quad (21a)$$

and

$$\mathcal{S}_o^{\pm}(\hat{\mathbf{k}},t,\hat{\mathbf{v}}) = \int_{S_o} dS'\, \hat{\mathbf{v}}\times\mathbf{S}_o(\mathbf{r}')\delta\left(t \pm \hat{\mathbf{k}}\cdot(\mathbf{r}' - \mathbf{r}_o^c)\Big/ c\right) \quad (21b)$$

where $o = \{m,n\}$.

Computing all interactions requires numerical implementation of (20a)–(20c). In practice, as all spherical integrals are computed using quadrature rules, it is necessary to temporally bandlimit the current densities. This follows naturally as the excitation is assumed to be bandlimited to $f_{\max}$. Thus, the current density can be locally interpolated using temporally bandlimited and approximately time-limited functions such that the time signature of the current for the lth time-slice can be written as

$$f_{n,l}(t) = \sum_{j=(l-1)M_t+1}^{lM_t} I_{n,j}\Psi_j(t) \quad (22)$$

where $\Psi_j(t) = \Psi(t - j\Delta_t)$ is an interpolant bandlimited to $f_s > f_{\max}$. In this study, $\Psi_j(t)$ is chosen to be a variant of the approximate prolate spheroidal functions [30] [see Fig. 4(b)]. Timelimiting these functions to a duration of $(2p+1)\Delta_t$ introduces an error which decreases exponentially with increasing p. As a result, $f_{n,l}(t)$ can be considered bandlimited and spans a duration $M_t'\Delta_t = (M_t + 2p)\Delta_t$. Evaluation of (20a)–(20c) is done by sampling on the surface of the sphere. As the far field is bandlimited, it is possible to show that the number of samples needed to completely characterize the field is of $\mathcal{O}(M^2)$, where

$$M = \mathrm{Int}(4\pi\chi f_s R_s/c) + 1 \quad (23)$$

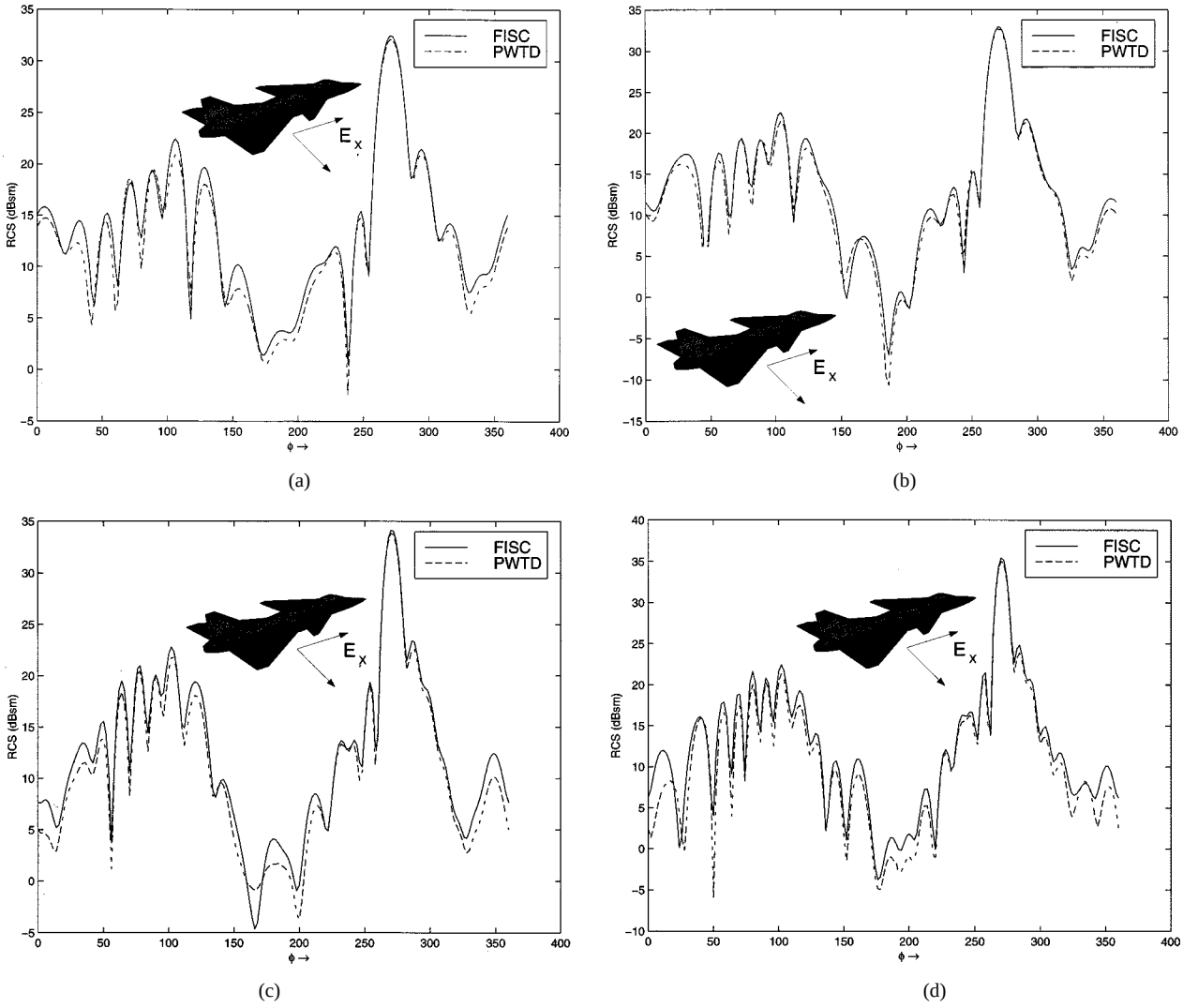

Fig. 10. Radar cross section of an aircraft (VFY 218) in the x-y plane extracted from the time-domain CFIE result is compared to that obtained from FISC for four different frequencies. The incident wave propagates along $\mathbf{k} = -\hat{\mathbf{y}}$ and is $\hat{\mathbf{p}} = \hat{\mathbf{x}}$ polarized and the cone sphere is discretized using 9747 spatial basis functions. (a) 75 MHz. (b) 85 MHz. (c) 105 MHz. (d) 130 MHz.

and χ is an oversampling factor [31], [32]. Note that the translation function (21a) can be succinctly expressed as $\mathcal{T}(\hat{\mathbf{k}}, t) = \hat{\mathcal{T}}(\hat{\mathbf{k}}, t, \infty)$, where [27]

$$\hat{\mathcal{T}}(\hat{\mathbf{k}}, t, \hat{M}) = \frac{c\partial_t^3}{2R_c} \sum_{\nu=0}^{\hat{M}} (2\nu+1) P_\nu \left(\frac{ct}{R_c}\right) P_\nu(\cos\theta'), \quad \text{for } |t| \le \frac{R_c}{c} \tag{24}$$

and $P_\nu(x)$ are Legendre polynomials of degree ν. In keeping with the bandlimitedness of the fields, the upper limit in the above summation can be truncated to $\hat{M} = M$ [33]. Consequently, (20a)–(20c) can be evaluated numerically using

$$\begin{aligned}\langle \mathbf{S}_m(\mathbf{r}), \mathcal{L}_e\{\mathbf{J}_{n,l}(\mathbf{r},t)\}\rangle &= \frac{\eta_0}{8\pi^2 c^2} \int_{T_{l,\text{stop}}}^{t} dt' \sum_{k=0}^{M} \sum_{p=-M}^{M} w_{kp} \\ &\times [\mathcal{S}_m^-(\hat{\mathbf{k}}_{kp}, t', \hat{\mathbf{k}}_{kp})]^T * \hat{\mathcal{T}}(\hat{\mathbf{k}}_{kp}, t', M) \\ &* [\mathcal{S}_n^+(\hat{\mathbf{k}}_{kp}, t', \hat{\mathbf{k}}_{kp})] * f_{n,l}(t') \end{aligned} \tag{25a}$$

$$\begin{aligned}\langle \mathbf{S}_m(\mathbf{r}), \mathcal{L}_h\{\mathbf{J}_{n,l}(\mathbf{r},t)\}\rangle &= \frac{1}{8\pi^2 c^2} \int_{T_{l,\text{stop}}}^{t} dt' \sum_{k=0}^{M} \sum_{p=-M}^{M} w_{kp} \\ &\times [\mathcal{S}_m^-(\hat{\mathbf{k}}_{kp}, t', \hat{\mathbf{n}})]^T * \hat{\mathcal{T}}(\hat{\mathbf{k}}_{kp}, t', M) \\ &* [\mathcal{S}_n^+(\hat{\mathbf{k}}_{kp}, t', \hat{\mathbf{k}}_{kp})] * f_{n,l}(t'). \end{aligned} \tag{25b}$$

The corresponding equation for the $\langle \mathbf{S}_m(\mathbf{r}), \mathcal{L}_c\{\mathbf{J}_{n,l}(\mathbf{r},t)\}\rangle$ can be obtained using (20c), and the time integral in the above equation is performed using standard integration rules [34]. In the above equations, w_{kp} are the quadrature weights [33] given by

$$w_{kp} = \frac{4\pi(1-\cos^2\theta_k)}{(2M+1)[(M+1)P_M(\cos\theta_k)]^2} \tag{26}$$

$$\hat{\mathbf{k}}_{kp} = \hat{\mathbf{x}}\sin\theta_k\cos\phi_p + \hat{\mathbf{y}}\sin\theta_k\sin\phi_p + \hat{\mathbf{z}}\cos\theta_k \tag{27}$$

$$\phi_p = 2\pi p/(2M+1) \quad \text{and} \tag{28}$$

$$\theta_k \text{ is the } (k+1)^{\text{th}} \text{ zero of } P_{M+1}(\cos\theta). \tag{29}$$

To gain insight into (25) note that the rightmost convolution maps the source distribution onto a set of plane waves which will henceforth be referred to as "outgoing rays." In the literature, this mapping is also known as the slant stack transform (SST)

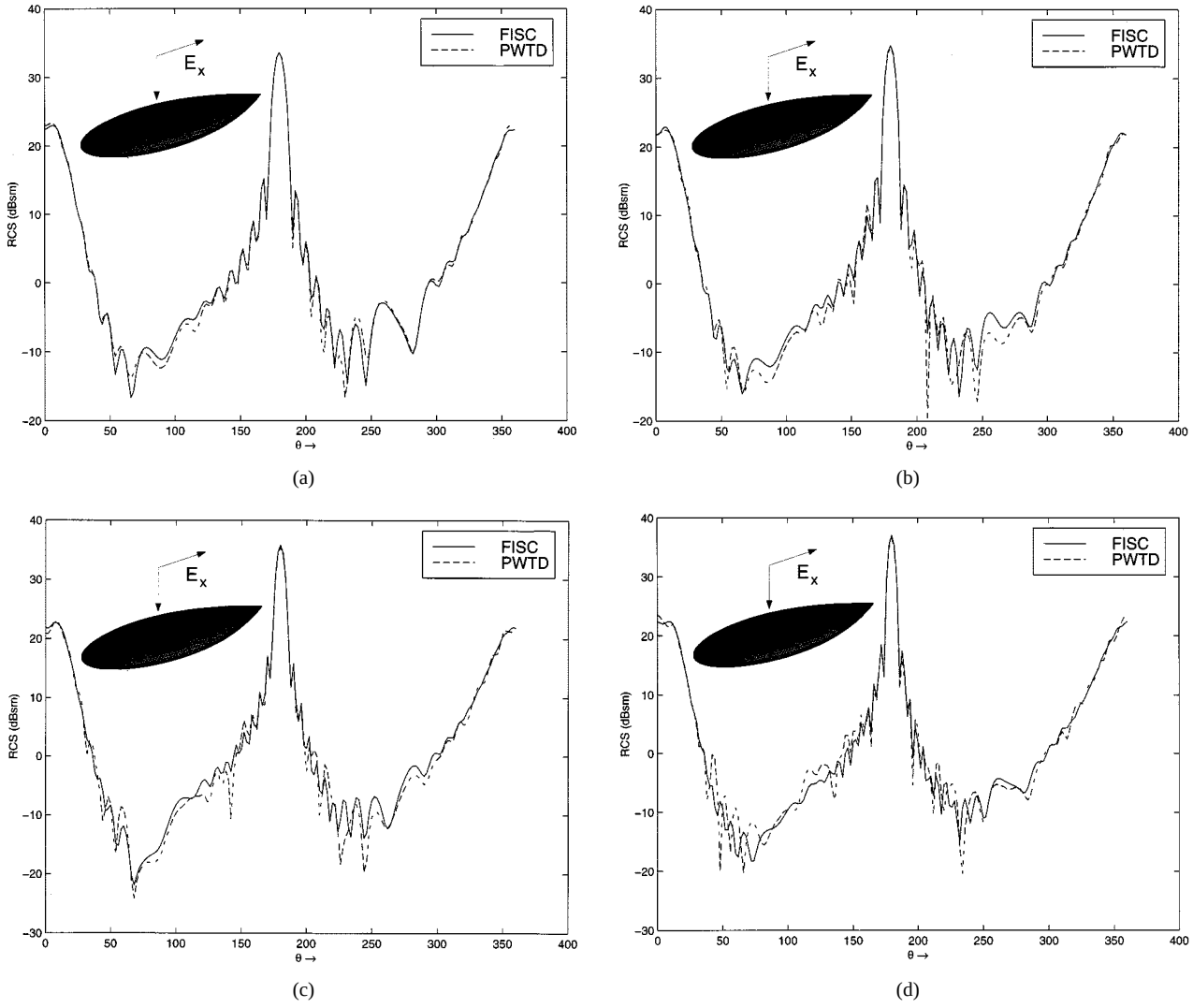

Fig. 11. Radar cross section of an almond in the z-x plane extracted from the time domain CFIE result is compared to that obtained from FISC for four different frequencies. The incident wave propagates along $\hat{\mathbf{k}} = -\hat{\mathbf{z}}$ and is $\hat{\mathbf{p}} = \hat{\mathbf{x}}$ polarized, and the almond is discretized using 29 700 spatial basis functions. (a) 400 MHz. (b) 460 MHz. (c) 520 MHz. (d) 600 MHz.

[29]. The center convolution "translates" these to "incoming rays," which impinge on the observation sphere. Finally, via the last convolution and the spectral integration the incoming rays are mapped onto the observers. The reconstruction of transient field using this three-stage process of aggregation, translation, and disaggregation, is reminiscent of the popular frequency-domain FMM.

B. Implementation of Two-Level PWTD Enhanced MOT Solvers

The ideas outlined in the preceding subsection give rise to a procedure via which the interaction between basis functions residing in any far-field box pair (α, α') can be computed as a superposition of transient plane waves. To complete the PWTD algorithmic prescription, these ideas are now systematized such that they can be efficiently applied in conjunction with an MOT scheme. With this in mind, a fundamental subsignal duration $T_s = (M_t + 2p)\Delta_t$ is defined, where

$$M_t = \min_{(\alpha,\alpha')} \left\{ \left\lfloor \frac{R_{c,\alpha\alpha'} - 2R_s}{c\Delta_t} \right\rfloor \right\} - 2p \tag{30}$$

and $R_{c,\alpha\alpha'}$ is the distance between the centers of the boxes (α, α'). Such a definition stems from the fact that T_s corresponds to the duration of the longest possible subsignal that can be translated "ghost-free" between the closest far-field pair. For all other far-field pairs, the subsignal lengths are chosen to be an integer multiple of the fundamental duration, i.e., $T_{s,\alpha\alpha'} = (M_{t,\alpha\alpha'} + 2p)\Delta_t$, where $M_{t,\alpha\alpha'} = M_t \lfloor (R_{c,\alpha\alpha'} - 2R_s - 2pc\Delta_t)/M_t \rfloor$. The rationale behind this choice will soon become transparent.

The task of computing the current distribution at each time step is divided into (i) evaluating near-field interactions using the usual MOT scheme and (ii) computing far-field interactions using the PWTD algorithm.

i) *Near-Field Evaluation*: at each time step, the sum

$$\sum_{i=1}^{j-1} \mathcal{Z}^i_{q,mn} \mathcal{I}_{j-i,n} \quad \forall m \in \alpha \quad \text{and} \quad \forall n \in \alpha' \tag{31}$$

is computed for all near-field interaction pairs (α, α').

ii) *Far-Field Evaluation*: to take all the far-field interactions into account, the algorithm follows the three stage process that was alluded to in the previous subsection.

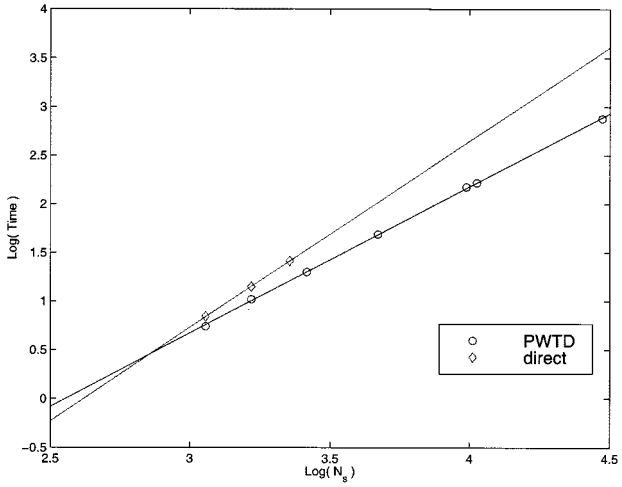

Fig. 12. Comparison of the computational complexity of the classical and PWTD augmented MOT schemes.

a) The first task is the construction of outgoing rays for all boxes. This involves computing $\mathcal{S}_n^+(\hat{\mathbf{k}}_{kp}, t, \hat{\mathbf{k}}_{kp})$ for all ray directions for a fundamental subsignals comprised of $M_t + 2p$ samples and a duration T_s. Note that once this information has been computed, it can be reused for different interaction pairs. Furthermore, the number of time slices for which one needs to store these outgoing rays is proportional to the largest linear dimension of the scatterer.

b) The next step is to translate the outgoing rays from a source group α' to an observer group α. This is done every $M_{t,\alpha\alpha'}$ time steps. As $M_{t,\alpha\alpha'}$ is an integer multiple of M_t, the rays to be translated can be formed by concatenating an appropriate number of outgoing rays from group α'. Since the length of the translation function is $2R_{c,\alpha\alpha'}/(c\Delta_t) = \mathcal{O}(M_{t,\alpha\alpha'})$ time steps, the convolution of the outgoing ray with the translation function can be efficiently accomplished using fast Fourier transforms (FFT's) since the length of the outgoing ray to be translated is of the same order. Unfortunately, as the translation function is not bandlimited, simple FFT's cannot be used to transform it into the Fourier domain. However, this hurdle can be surmounted as an analytical expression for the Fourier transform of the translation function is available. For a far-field pair (α, α'), the Fourier transform of the translation function is

$$\begin{aligned}\breve{\mathcal{T}}(\hat{\mathbf{k}}, \omega) &= \int_{-\infty}^{\infty} dt\, e^{-j\omega t} \hat{\mathcal{T}}(\hat{\mathbf{k}}, t, \hat{M}) \\ &= \int_{-\infty}^{\infty} dt\, e^{-j\Omega_f ct/R_{c,\alpha\alpha'}} \hat{\mathcal{T}}(\hat{\mathbf{k}}, t, \hat{M}) \\ &= -\frac{jc^3}{R_{c,\alpha\alpha'}^3} \Omega_f^3 \sum_{\nu=0}^{\hat{M}} (2\nu+1)(-j)^\nu j_\nu(\Omega_f) P_\nu(\cos\theta) \\ &= -\frac{jc^3}{R_{c,\alpha\alpha'}^3} \tilde{\mathcal{T}}(\hat{\mathbf{k}}, \Omega_f) \end{aligned} \tag{32}$$

where $\Omega_f = \omega R_{c,\alpha\alpha'}/c$ is the normalized frequency and $j_\nu(\cdot)$ is a spherical Bessel function of the νth order [27]. This equation also indicates that the translation function for an arbitrary sphere pair can be constructed from a function $\tilde{\mathcal{T}}(\hat{\mathbf{k}}, \Omega_f)$ that is bandlimited in both the Ω_f and θ. Hence, this function can be sampled at a discrete set of points and the translation function for any far-field sphere pair reconstructed by interpolating through these samples. After convolving the outgoing rays with the translation function, the resulting rays are then superimposed on to the incoming rays of the observer group. It should be noted that as the evaluation of $\mathcal{S}_n^+(\hat{\mathbf{k}}_{kp}, t, \hat{\mathbf{k}}_{kp})$ yields two real signals, viz., the $\hat{\theta}$ and $\hat{\phi}$ components of the field which are to be translated, this operation is most efficiently performed using one complex FFT [34].

c) Finally, the rays entering all the spheres are projected on to the observers. This is done via the leftmost convolution in (25).

It should be pointed out that the error incurred in computing the fields via a plane wave expansion method can be controlled to arbitrary precision [17], [33].

C. Complexity Analysis

To analyze the computational complexity of the PWTD-enhanced MOT solver described above, assume that there are N_g nonempty boxes, each containing approximately $M_s = N_s/N_g$ unknowns. In what follows, implementation dependent constants are denoted as C_i, $i = 0, 1, 2, 3$. The cost of a PWTD-MOT analysis is comprised of near- and far-field components. The computation of all near field interactions for the duration of the analysis requires

$$C_{\mathrm{NF}} = C_0 N_g M_s^2 N_t \tag{33a}$$

operations. The cost of evaluating all far field interactions consists of those incurred in constructing outgoing rays (C_{FF}^1), translating the latter onto incoming rays (C_{FF}^2), and projecting incoming rays onto observers (C_{FF}^3). Constructing outgoing rays involves the projection of all current elements in the N_g nonempty boxes onto $\mathcal{O}(M^2) = \mathcal{O}(M_s)$ plane waves for all N_t time steps. Projecting incoming rays onto observers involves a very similar set of operations. Hence, the cost associated with these operations is

$$C_{\mathrm{FF}}^{1,3} = C_{1,3} N_g M_s^2 N_t. \tag{33b}$$

The cost of translating one ray between groups (α, α') scales as $\mathcal{O}(M_{t,\alpha\alpha'} \log M_{t,\alpha\alpha'})$. As this operation has to be performed for all $N_t/M_{t,\alpha\alpha'}$ time slices and $\mathcal{O}(M^2) = \mathcal{O}(M_s)$ directions, the cost of translating information between a given pair of spheres for the duration of the analysis scales as $\mathcal{O}(N_t M^2 \log M_{t,\alpha\alpha'})$. Since $M_{t,\alpha\alpha'}$ is bounded by the maximum linear dimension of the scatterer ($\sqrt{N_s}$), the cost of translations for all N_g^2 far-field group interactions is

$$C_{\mathrm{FF}}^2 = C_2 N_t N_s^2 / M_s \log N_s. \tag{33c}$$

The total cost associated with the PWTD-enhanced MOT analysis is

$$C_T = C_{\mathrm{NF}} + C_{\mathrm{FF}}^1 + C_{\mathrm{FF}}^2 + C_{\mathrm{FF}}^3. \tag{34}$$

Minimizing C_T with respect to M_s reveals that the optimal number of unknowns per group grows as $M_s \propto N_s^{1/2}$ and that C_T scales as $\mathcal{O}(N_t N_s^{3/2} \log N_s)$.

IV. Numerical Results

This section presents numerical results that serve both to validate the above described PWTD-enhanced MOT scheme and to demonstrate its efficacy. The algorithm is verified in two stages. In a first set of simulations, scattering from electrically small structures is analyzed using PWTD-enhanced and classical EFIE- and MFIE-based MOT codes and compared in the time domain directly. In a second set of simulations, frequency-domain radar cross section (RCS) data is extracted from the Fourier transformed temporal far-field signatures [22] obtained using a PWTD-augmented CFIE-based MOT solver. This data is compared against similar results obtained using the fast Illinois solver code (FISC), an FMM-based CFIE frequency-domain [16] code. In all the examples presented herein, the incident pulse is a modulated Gaussian plane wave parameterized as

$$\mathbf{E}^i(\mathbf{r},t) = \hat{\mathbf{p}}\cos(2\pi f_0[t-\mathbf{r}\cdot\hat{\mathbf{k}}/c]) \times \exp\left[-\frac{(ct-\mathbf{r}\cdot\hat{\mathbf{k}}-ct_p)^2}{2\sigma^2c^2}\right] \tag{35}$$

where f_0 is the pulse's center frequency, $\hat{\mathbf{k}}$ and $\hat{\mathbf{p}}$ denote its direction of travel and polarization, $\sigma = 6/(2\pi f_{\rm bw})$, and $t_p = 3.5\sigma$. The parameter $f_{\rm bw}$ will be referred to as the "bandwidth" of the signal. It is to be noted that the power in the incident pulse is down by 160 dB at $f = f_0 \pm f_{\rm bw}$ relative to f_0. Also, the details on the geometries of some of the scatterers that are used here to illustrate the capabilities of this code can be obtained from [35].

To establish that both PWTD-enhanced and classical MOT schemes yield identical results, transient scattering from two objects is analyzed. The first object is a rectangular plate of dimensions 2 m $\times$15 m that resides in the x-y plane. A $\hat{\mathbf{p}} = \hat{\mathbf{x}}$ polarized pulse traveling in the $\hat{\mathbf{k}} = -\hat{\mathbf{z}}$ direction, with center frequency $f_0 = 100$ MHz and bandwidth $f_{\rm bw} = 50$ MHz is incident on the plate. The current on the plate is represented using 2170 spatial basis functions and solved for using the EFIE. The magnitudes of the current at $(0.2, 2.0, 0.0)$ on the plate's surface, computed using both the PWTD-enhanced and classical MOT schemes are compared in Fig. 5(a). Similarly, the temporal far field signatures of the field scattering along $+\hat{\mathbf{z}}$, computed using both methods, are compared in Fig. 5(b). Obviously, our PWTD-enhanced MOT solver yields results that agree very well with those obtained using the classical scheme.

The second object studied is an almond that fits into a rectangular box of size 5.00 m $\times$ 1.92 m $\times$ 0.64 m. The almond is excited by a pulse traveling along $\hat{\mathbf{k}} = -\hat{\mathbf{z}}$ and polarized along $\hat{\mathbf{p}} = \hat{\mathbf{x}}$. The center frequency and bandwidth of the pulse are $f_0 = 204$ and $f_{\rm bw} = 200$ MHz, respectively. The current on the almond is represented using 4680 spatial basis functions and solved for using an MFIE. Figs. 6(a) and (b) compare the magnitude of the current at $(0.01, 0.58, 0.03)$ on the almond and the far field signature of the $+\hat{\mathbf{z}}$ traveling scattered field obtained using PWTD-enhanced and classical MOT codes; again, good agreement between both sets of results is observed.

Via the above numerical simulations, it has been verified that the solutions to the EFIE and the MFIE obtained using PWTD-enhanced and classical MOT schemes are in agreement. Next, the PWTD-accelerated MOT codes is applied to the analysis of scattering from electrically large objects and is further validated by comparing their bistatic RCS extracted at a number of frequency points against RCS data computed using a frequency-domain solver. In all the examples that follow, the time-domain CFIE is used as the solution to the time-domain EFIE and MFIE can be corrupted by internal resonance modes [20]. First, transient scattering from a sphere of unit radius is analyzed. The sphere is illuminated by a modulated Gaussian pulse traveling in the $\hat{\mathbf{k}} = -\hat{\mathbf{z}}$ direction and polarized along $\hat{\mathbf{p}} = \hat{\mathbf{x}}$. The center frequency and bandwidth of the pulse are $f_0 = 400$ MHz and $f_{\rm bw} = 200$ MHz, respectively, and the sphere is discretized using 9414 spatial basis functions. Figs. 7(a)–(d) compare the RCS pattern in the x-z plane obtained using the PWTD-enhanced MOT scheme and FISC for a range of frequencies within the band of excitation. Specifically, the RCS is compared at 280, 350, 420 and 500 MHz. Results obtained from the time and frequency domain codes are in good agreement with each other, even at 280 and 500 MHz, where the power in the incident pulse is down by 65 and 40 dB from its peak at f_0, respectively. In this and subsequent examples, comparisons at frequencies where the power is down by at least 30 dB are made to highlight the fact that meaningful results can be obtained at these points through the use of the CFIE. Indeed, if either the MFIE or the EFIE were used, errors induced by nonphysical currents at resonance frequencies would propagate in any MOT scheme and would be most visible at the ends of the band [20].

Next, transient scattering from an almond that fits into a rectangular box of dimensions 5.0 m $\times$ 1.92 m $\times$ 0.64 m is analyzed. A pulse traveling along $\hat{\mathbf{k}} = -\hat{\mathbf{z}}$ and polarized along $\hat{\mathbf{p}} = \hat{\mathbf{x}}$ excites the almond. The center frequency and bandwidth of the pulse are $f_0 = 303.4$ and $f_{\rm bw} = 200$ MHz, respectively, and the almond is discretized using 10 620 spatial basis functions. RCS patterns in the x-z plane are extracted from temporal far-field signatures at 210.2, 261.8, 322.0, and 390.8 MHz, and compared against FISC data in Fig. 8(a)–(d); again, all RCS patterns agree well with each other. It should also be pointed out that at both 210.2 and 390.8 MHz the power in the incident pulse is down by about 30 dB from its peak at f_0.

Next, scattering from a cone sphere is studied. The cone is 1 m long and the radius of the half sphere attached to the cone is 0.235 m. The incident pulse has a center frequency of $f_0 = 800$ and bandwidth $f_{\rm bw} = 750$ MHz is $\hat{\mathbf{p}} = \hat{\mathbf{z}}$ polarized and travels along the $\hat{\mathbf{k}} = -\hat{\mathbf{y}}$ direction. This cone sphere is discretized using 11 412 spatial basis functions. The RCS patterns in the y-z plane obtained from the time-domain PWTD-enhanced MOT code is compared against that obtained from FISC 500, 700, 900, 1100 MHz, as shown in Fig. 9(a)–(d). Examination of Fig. 9(a)–(d) shows that both the FISC and the PWTD results agree very well with each other, even at 500 and 1100 MHz where the power in the incident pulse is down by 25 dB from that at 750 MHz.

All examples analyzed thus far involved relatively simple geometries. Next, scattering from a VFY 218 aircraft, discretized using 9747 spatial basis functions is analyzed. The incident field travels in the $\hat{\mathbf{k}} = -\hat{\mathbf{y}}$ direction and is polarized along $\hat{\mathbf{p}} = \hat{\mathbf{x}}$, has a center frequency of $f_0 = 100$ MHz and bandwidth of $f_{\rm bw} = 60$ MHz. Fig.10(a)–(d) compares the RCS patterns in

the x-y plane at 75, 85, 105, and 130 MHz, where the pulse's power at these frequencies is down by 27, 9.7, 1.07, and 39 dB with respect to its peak value. Again, the results of the time-domain code replicate all of the RCS nulls and peaks computed using the frequency-domain solver.

Finally, scattering from an almond discretized with 29 700 spatial basis functions is analyzed. This simulation pushes the limits of the two-level PWTD algorithm insofar as computational resources are concerned. This almond fits inside a rectangular box of dimensions 6.00 m $\times$ 2.31 m $\times$ 0.77 m and is illuminated by a $\hat{\mathbf{p}} = \hat{\mathbf{x}}$ polarized Gaussian pulse traveling along $\hat{\mathbf{k}} = -\hat{\mathbf{z}}$, with a center frequency of $f_0 = 500$ MHz and a bandwidth of $f_{\rm bw} = 300$ MHz. Fig.11(a)–(d) compares the RCS pattern in the x-z plane computed using the time- and frequency-domain codes at 400, 460, 520, and 600 MHz. At both 400 and 600 MHz, power in the incident field is down by 27 dB from its peak. As is apparent in Figs. 11(a)–(d) , the RCS patterns computed by both the time-domain and frequency-domain codes are in very good agreement with each other.

Finally, the predicted computational complexity of both the PWTD-enhanced and classical MOT schemes is verified. All results presented above were obtained using an SGI Origin2000 with peak performance rated at 360 Mflops. In Fig. 12, the logarithm of the central processing unit (CPU) time required to compute the interactions at one time point is plotted against the $\log N_s$. This graph reveals that the computational cost of a PWTD-MOT algorithm scales as $\mathcal{O}(N_t N_s^{1.507} \log N_s)$, which is very close to the theoretically predicted scaling law. Also, it should be noted that the break-even point or the number of unknowns where it becomes more advantageous to use the PWTD-enhanced MOT schemes as opposed to a classical MOT solver, is as low as $N_s = 700$.

V. Conclusion

This paper presented a two-level PWTD-enhanced MOT algorithm that permits the fast EFIE-, MFIE-, and CFIE-based analysis of transient electromagnetic scattering phenomena. The computational complexity of this algorithm scales as $\mathcal{O}(N_t N_s^{3/2} \log N_s)$, as opposed to $\mathcal{O}(N_t N_s^2)$ for the conventional MOT algorithm. Numerous simulations that were conducted during the course of this study demonstrate the usefulness of these solvers in characterizing broad-band scattering from large objects.

Acknowledgment

The authors would like to thank J. M. Song and W. C. Chew for granting access to FISC technology and NCSA for use of its computational facilities.

References

[1] A. Taflove, *Computational Electrodynamics: The Finite Difference Time Domain Method*. Boston, MA: Artech House, 1995.

[2] K. S. Kunz and R. J. Luebbers, *The Finite Difference Time Domain Method for Electromagnetics*. Boca Raton, FL: CRC, 1993.

[3] C. L. Bennet, "A technique for computing approximate impulse response for conducting bodies," Ph.D. Thesis, Purdue Univ., West Lafayette, IN, 1968.

[4] A. J. Poggio and E. K. Miller, *Computer Techniques for Electromagnetics*. Oxford, U.K.: Pergamon, 1973, ch. 4.

[5] R. Mittra, *Transient Electromagnetic Fields*. New York: Springer-Verlag, 1976, ch. 2.

[6] B. P. Rynne and P. D. Smith, "Stability of time marching algorthms for the electric field integral equations," *J. Electromagn. Waves Applicat.*, vol. 12, pp. 1181–1205, 1990.

[7] E. K. Miller, "A selective survey of computational electromagnetics," *IEEE Trans. Antennas Propagat.*, vol. 36, pp. 1281–1305, Sept. 1988.

[8] A. G. Tijhuis, *Electromagnetic Inverse Profiling*. Utrecht, The Netherlands: VNU Sci., 1987.

[9] D. A. Vechinski and S. M. Rao, "A stable procedure to calculate the transient scattering by conducting surfaces of arbitrary shape," *IEEE Trans. Antennas Propagat.*, vol. 40, pp. 661–665, June 1992.

[10] B. P. Rynne, "Stability and convergence of time marching methods in scattering problems," *Int. J. Appl. Math.*, vol. 35, pp. 297–310, 1985.

[11] W. Pinello, A. Ruehli, and A. Cangellaris, "Stabilization of time domain solutions of the efie based on the partial element equivalent circuit models," in *Proc. IEEE Antennas Propagat. Soc. Int. Symp.*, vol. 3, Montreal, Canada, July 1997, pp. 966–969.

[12] M. J. Bluck and S. P. Walker, "Time-domain BIE analysis of large three dimensional electromagnetic scattering problems," *IEEE Trans. Antennas Propagat.*, vol. 45, pp. 894–901, May 1997.

[13] S. Dodson, S. P. Walker, and M. J. Bluck, "Implicitness and stability of time domain integral equation scattering analysis," *Appl. Comp. Electromagn. Soc. J.*, vol. 13, no. 3, pp. 291–301, 1998.

[14] S. P. Walker, "Scattering analysis via time-domain integral equations: Methods to reduce the scaling of cost with frequency," *IEEE Antennas Propagat. Mag.*, vol. 39, pp. 13–20, Oct. 1997.

[15] R. Coifman, V. Rokhlin, and S. Wandzura, "The fast multipole method for the wave equation: A pedestrian prescription," *IEEE Antennas Propagat. Mag.*, vol. 35, pp. 7–12, June 1993.

[16] J. M. Song, C. C. Lu, and W. C. Chew, "MLFMA for electromagnetic scattering by large complex objects," *IEEE Trans. Antennas Propagat.*, vol. 45, pp. 1488–1493, Oct. 1997.

[17] A. A. Ergin, B. Shanker, and E. Michielssen, "Fast evaluation of transient wave fields using diagonal translation operators," *J. Comp. Phys.*, vol. 146, pp. 157–180, 1998.

[18] A. A. Ergin, B. Shanker, and E. Michielssen, "Fast transient analysis of acoustic wave scattering from rigid bodies using a two-level plane wave time domain algorithm," *J. Acoust. Soc. Amer.*, vol. 106, pp. 2405–2416, 1999.

[19] J. R. Mautz and R. F. Harrington, "H-field, e-field, and combined field solutions for conducting bodies of revolution," *AEÜ*, vol. 32, pp. 157–164, 1978.

[20] B. Shanker, A. A. Ergin, K. Agyün, and E. Michielssen, "Analysis of transient electromagnetic scattering from closed surfaces using the combined field integral equation," IEEE Trans. Antennas Propagat., to be published.

[21] D. S. Jones, *Methods in Electromagnetic Wave Propagation*. Oxford, U.K.: Oxford Sci., 1994.

[22] S. M. Rao and D. R. Wilton, "Transient scattering by conducting surfaces of arbitrary shape," *IEEE Trans. Antennas Propagat.*, vol. 39, pp. 56–61, 1991.

[23] S. M. Rao, D. R. Wilton, and A. W. Glisson, "Electromagnetic scattering by surfaces of arbitrary shape," *IEEE Trans. Antennas Propagat.*, vol. AP-30, pp. 408–418, May 1982.

[24] P. D. Smith, "Instabilities in time marching methods for scattering: Cause and rectification," *Electromagn.*, vol. 10, pp. 439–451, 1990.

[25] G. Manara, A. Monorchio, and R. Reggiannini, "A space-time discretization criterion for a stable time-marching solution of the electric field integral equation," *IEEE Trans. Antennas Propagat.*, vol. 45, pp. 527–532, Mar. 1997.

[26] Y. Saad, *Iterative Methods for Sparse Linear Systems*. New York: PWS, 1996.

[27] M. Abramowitz and I. A. Stegun, *Handbook of Mathematical Functions*. New York: Dover, 1972.

[28] M. Tygel and P. Hubral, *Transient Waves in Layered Media*. Amsterdam, The Netherlands: Elsevier, 1987.

[29] E. Heyman, "Time-depenent plane-wave spectrum representations for radiation from volume source distributions," *J. Math. Phys.*, vol. 37, pp. 658–681, 1996.

[30] J. J. Knab, "Interpolation of bandlimited functions using the approximate prolate series," *IEEE Trans. Inform. Theory*, vol. IT-25, pp. 717–720, Nov. 1979.

[31] O. M. Bucci and G. Franceschitti, "On the spatial bandwidth of scattered fields," *IEEE Trans. Antennas Propagat.*, vol. AP-35, pp. 1445–1455, Dec. 1987.
[32] O. M. Bucci, C. Gennarelli, and C. Savarse, "Optimal interpolation of radiated fields over a sphere," *IEEE Trans. Antennas Propagat.*, vol. 39, pp. 1633–1643, Nov. 1991.
[33] A. A. Ergin, B. Shanker, and E. Michielssen, "The plane wave time domain algorithm for the fast analysis of transient wave phenomena," *IEEE Antennas Propag. Mag.*, vol. 41, pp. 39–52, Aug. 1999.
[34] W. H. Press, S. A. Teukolsky, W. T. Vetterling, and B. P. Flannery, *Numerical Recipies in Fortran 77*, Cambridge, U.K.: Cambridge Univ. Press, 1992.
[35] A. C. Woo, H. T. G. Wang, M. J. Schuh, and M. L. Sanders, "Benchmark radar targets for the validation of computational electromagnetics programs," *IEEE Antennas Propagat. Mag.*, vol. 35, pp. 84–89, Aug. 1993.

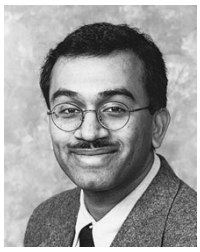

Balasubramaniam Shanker (M'96) received the B.Tech. degree from the Indian Institute of Technology, Madras, India, in 1989, and the M.S. and Ph.D. degrees from the Pennsylvania State University, State College, PA, in 1992 and 1993, respectively.

From 1993 to 1996, he was a Research Associate in the Department of Biochemistry and Biophysics, Iowa State University, Ames, where he worked on the molecular theory of optical activity. From 1996 to 1999 he was with the Center for Computational Electromagnetics at the University of Illinois at Urbana-Champaign, first as a Research Associate and then as a Visiting Assistant Professor. He is currently an Assistant Professor in the Department of Electrical and Computer Engineering, Iowa State University. He has published over 35 journal articles and over 40 conference papers/presentations. His research interests include all aspects of computational electromagnetics with an emphasis of fast time and frequency-domain algorithms.

Dr. Shanker is listed in *Who's Who in Science and Engineering*. He is a member of the IEEE Optical Society of America (OSA) technical societies.

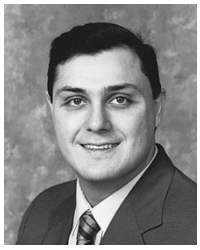

A. Arif Ergin (S'91) received the B.S. degree from the Middle East Technical University, Ankara, Turkey, in 1992, and the M.S. degree from the University of Illinois at Urbana-Champaign, in 1995. He is currently working toward the Ph.D. degree at the University of Illinois at Urbana-Champaign.

He worked as a Design Engineer in ASELSAN Inc., Ankara, Turkey, from 1992 to 1993. He is currently a Research Assistant at the Center for Computational Electromagnetics, University of Illinois. His current research interests include computational methods for analyzing wave propagation and scattering in acoustics and electromagnetics.

Mr. Ergin is a member of ASA.

Kemal Aygün (S'99) received the B.S. degree from the Middle East Technical University, Ankara, Turkey, in 1995, and the M.S. degree from the University of Illinois at Urbana-Champaign, in 1997, both in electrical engineering. He is currently working toward the Ph.D. degree from University of Illinois at Urbana-Champaign.

Since 1995, he has been a Research Assistant at the Center for Computational Electromagnetics, University of Illinois. His research is currently focused on the numerical solution of electromagnetic scattering and radiation problems.

Mr. Aygün is the recipient of the 1999 Computational Science and Engineering Fellowship.

Eric Michielssen (M'95–SM' 99) received the M.S. degree in electrical engineering (*summa cum laude*) from the Katholieke Universiteit Leuven (KUL, Belgium), in 1987, and the Ph.D. degree in electrical engineering from the University of Illinois at Urbana-Champaign (UIUC), in 1992.

He served as a Research and Teaching assistant in the Microwaves and Lasers Laboratory at KUL and the Electromagnetic Communication Laboratory, UIUC, from 1987 to 1988 and from 1988 to 1992, respectively. He joined the Faculty of the Department of Electrical and Computer Engineering, University of Illinois, as a Visiting Assistant Professor in 1992, was appointed Assistant Professor of Electrical and Computer Engineering in 1993, and was promoted to Associate Professor in 1998. Since 1995 he has served as Associate Director of the Center for Computational Electromagnetics at UIUC. From 1997 to 1999 he served as an associate editor for *Radio Science*. He authored or coauthored over 65 papers and book chapters and over 100 papers in conference proceedings. His research interests include all aspects of theoretical and applied computational electromagnetics and his principal research focus has been on the development of fast-frequency and time-domain integral equation-based techniques for analyzing electromagnetic phenomena and the development of robust genetic algorithm driven optimizers for the synthesis of electromagnetic devices.

Dr. Michielssen received a Belgian American Educational Foundation Fellowship in 1988 and a Schlumberger Fellowship in 1990. He was the recipient of a 1994 Union of Radio Scientists International (URSI) Young Scientist Fellowship, a 1995 National Science Foundation CAREER Award, and the 1998 Applied Computational Electromagnetics Society (ACES) Valued Service Award. Recently, he was named 1999 URSI—United States National Committee Henry G. Booker Fellow and selected as the recipient of the 1999 URSI Koga Gold Medal. He served as the Technical Chairman of the 1997 Applied Computational Electromagnetics Society (ACES) Symposium (Review of Progress in Applied Computational Electromagnetics, March 1997, Monterey, CA), and currently he serves on the ACES Board of Directors. He currently is an associate editor for the IEEE TRANSACTIONS ON ANTENNAS AND PROPAGATION. He is a member of URSI Commission B.